PCCP

Accepted Manuscript

ROYAL SOCIETY OF CHEMISTRY

www.rsc.org/pccp

Graphene-coupled Bi_2WO_6 nanocomposite with enhanced photocatalytic performance: First-principles study

Fengzhu Ren[a], Jihua Zhang[a,b,*], Yuanxu Wang[a,b,*] , Wenzhi Yao[a,c]

[a]Institute for Computational Materials Science, School of Physics and Electronics, Henan University, Kaifeng 475004, China

[b]Guizhou Provincial Key Laboratory of Computational Nano-Material Science, Guizhou Education University, 115 Gaoxin Road, Guiyang 550018, China.

[c]Department of Environmental and Municipal Engineering, North China University of Water Conservancy and Electric Power, Zhengzhou 450011, China.

E-mail: wuli8@163.com, wangyx@henu.edu.cn.

Abstract: Experimentally synthesized graphene/Bi_2WO_6 composite showed an enhancement of the visible-light photocatalytic activity, while the underlying mechanism is not known. Here, first-principles calculations based on density functional theory were performed to explore the various properties of graphene/Bi_2WO_6 (010) composite aiming at gaining insights into the mechanism of photocatalytic performance. The stability, electronic properties, charge transfer, and visible-light response were investigated in detail on the Bi_2WO_6 (010) surface coupled with graphene. An analysis of charge distribution and Bader charge shows that there is a strong covalent bonding between graphene and Bi_2WO_6 (010) surface. The covalent interaction induces a small bandgap in graphene. The interband transition of graphene and the surface states of Bi_2WO_6 (010) surface would cause the absorption spectrum of the graphene/Bi_2WO_6 (010) covering the entire visible-light region and even infrared-light region. The photogenerated electrons flow to graphene from the conduction band of Bi_2WO_6 under the built-in electric field and band edge potential well. Thus, graphene serves as a photogenerated electron collector and transporter which significantly reduce the probability of electron-hole recombination and increase catalytic reaction sites not only on the surface of graphene but on also the surface of Bi_2WO_6. Decrease of charge recombination is possibly responsible for the enhancement of the visible-light photocatalytic activity in the graphene/Bi_2WO_6 (010) nanocomposite.

1. Introduction

TiO_2 is considered to be the most suitable photocatalyst due to its high photostability, nontoxicity, chemical robustness, and low cost [1, 2]. However, the wide band gap and low quantum efficiency of TiO_2 limit its practical applications. It is highly desirable for exploring effective photocatalysts with strong visible-light absorption, high thermal stability, and facilitating the separation and transfer of the photogenerated carriers. The bismuth-based oxides are good candidates as visible-light photocatalyst due to their chemical and thermal stability and nontoxicity [3]. Among them, the bismuth tungstate (Bi_2WO_6) is an effective visible-light-driven photocatalyst owing to its relatively narrow band gap (2.75 eV) and layer structure [4]. However, the photocatalytic activity of Bi_2WO_6 is still relatively low due to the rapid recombination of photogenerated electron–hole pairs and unsuitable conduction band edge position [5-7]. Cocatalyst modification with noble metals, such as Ag, Au, and Pt, is an efficient strategy to improve the photocatalytic efficiency of Bi_2WO_6 by enhancing light absorption ability and/or promoting the effective separation of photogenerated electrons and holes [8-10]. Nevertheless, noble metals are rare and expensive, limiting their wide application.

Graphene is an efficient cocatalyst due to its excellent mobility of charge carriers at room temperature ($\sim 2.0 \times 10^5$ $cm^2V^{-1}s^{-1}$) and extremely high theoretical specific surface area ($\sim 2.6 \times 10^3$ m^2g^{-1}). When graphene is coupled with semiconductor, the capture electronic Schottky barrier will be formed at the interface between graphene and semiconductor. Under light irradiation, the photogenerated electrons of graphene-semiconductor composites are captured by graphene and quickly transfer to the surface of graphene, which may suppress electron-hole recombination. Therefore, graphene-based semiconductor composite photocatalysts have been extensively applied to photocatalytic degradation of organic compounds[11-16]. These composite photocatalysts exhibit significant enhancement of photocatalytic activity compared with the corresponding bare photocatalysts. Very recently, the graphene/Bi_2WO_6 (010) composite has also been found to display an enhanced visible-light photocatalytic activity (such as, removing Rhodamine B, NO, phenol, Cr (VI), *etc* and generating H_2, O_2 from or in water or air) [17-22]. However, the photocatalytic performances of different samples are different depending on precursors or preparation methods. The origin of the enhanced photocatalytic performance is not well known. Thus it is desirable to explore factors for determining the photocatalytic properties of graphene/Bi_2WO_6

(010) composite and the interaction between graphene and Bi_2WO_6.

In the present work, the structure, stability, electronic properties, and visible-light response of the graphene/Bi_2WO_6 (010) composite have been systematically investigated to understand the mechanisms of its high photocatalytic activity. We found that the photogenerated electrons would flow to graphene from Bi_2WO_6 due to the higher conduction band edge of Bi_2WO_6 and a built-in electric field between graphene and Bi_2WO_6 after graphene is coupled with Bi_2WO_6. Thus, graphene can efficiently capture and transport photogenerated electrons, which will efficiently separate the photogenerated electron-hole pairs. The effective electron-hole separation is beneficial to improve the photocatalytic activity of the graphene/Bi_2WO_6 (010) composite, explaining well the high photocatalytic performances reported by experimental workers [19, 21].

2. Computational Details

Our calculations were performed with the projector-augmented wave (PAW) method [23]implemented in the Vienna *Ab initio* Simulation Package (VASP) [24, 25]. The generalized gradient approximation (GGA) [26] in the scheme of Perdew-Burke-Ernzerhof (PBE) [27] is used for the exchange-correlation functional. The explicit inclusion of the outer core *d* shells of the bismuth (the 5*d* states) and the 5*p* core shells of the tungsten little affect lattice parameters, bond lengths, and bond angles [28, 29]. Thus, the PAW potentials with the valence states 6*s*6*p* for Bi, 2*s*2*p* for O, 5*d*6*s* for W, 2*s*2*p* for C, have been employed. The cutoff energy was set to be 500 eV. The stopping criterion for electronic self-consistent interactions is convergence of the total energy to within 1×10^{-6} eV. Geometry relaxations were performed until the forces on each ion converged to be less than 0.02 eV/ Å.

Under normal conditions, Bi_2WO_6 crystallizes to the orthorhombic crystal structure with space group of Pca2(1), No. 29. Its lattice constants are a = 5.4326 Å, b = 16.4302 Å, c = 5.4584 Å [30]. The initial structure model of Bi_2WO_6 was constructed according to the experimental lattice parameters and the atomic positions. The optimized structural parameters as shown in our previous paper [6] are in excellent agreement with the experimental results, which indicated that the method in our calculation was reasonable. The composite is modeled by an interface with 15 Å vacuum on top. We consider the orthorhombic graphene/Bi_2WO_6 (010) composite, as Bi_2WO_6 (010) observed experimentally is the basal face [4]. In our composite model, the O-terminated Bi_2WO_6 (010) slab is expanded into 3×1 as the substrate to support

graphene with $4\sqrt{3} \times 2$ unit cell, in which the lattice mismatch rates along a and b orientation are about 4.3% and 10%, respectively. We also tried to deform Bi_2WO_6 (010) and to make it match graphene to form Bi_2WO_6 (010)/graphene composite. However, the calculated adhesion energy of Bi_2WO_6 (010)/graphene composite is larger than that of graphene/Bi_2WO_6 (010) composite. Therefore, we only consider the case of graphene/Bi_2WO_6 (010) in the following sections. The surface area of Bi_2WO_6 (010) surface is 5.44×5.46 Å^2. The Bi_2WO_6 (010) surface was also constructed with two Bi_2O_2 layers and a WO_6 layer and the surface energy convergence test indicated this surface was thick enough. In all calculations, the atoms in the seven bottom layers were fixed to simulate the bulk region, while the atoms in the four top layers, as well as the adsorbed graphene, were allowed to relax. The integrations over the Brillouin zone were performed by Monkhorst-Pack grids [31]. We used k-points meshes of $12 \times 4 \times 12$ for a Bi_2WO_6 unit cell, $40 \times 40 \times 1$ for a graphene unit cell, $12 \times 12 \times 1$ for Bi_2WO_6 (010) surface, and $4 \times 12 \times 1$ for the graphene/Bi_2WO_6 (010) composite. The dipole correction[32, 33] was applied to make the computation converge more quickly and eliminate the artificial electrostatic field between periodic supercells. Due to the well-known shortcoming of the DFT–GGA exchange correction functional in describing excited states, we adopted the GGA + U method of Dudarev *et al*'s approach [34] to partially correct this issue, and where the U parameter (Ueff = 3 eV [35] for the W 5d orbits) was used. Although a more accurate approach is to adopt hybrid functional[36], where the Hartree–Fock exchange is partially mixed with the DFT exchange, it would be prohibitively expensive from a computational point of view, since there are too many orbitals in this material for Hartree–Fock need to be dealt with. Moreover, because of strong chemical bonding between graphene and Bi_2WO_6 (010) surface, van der Waals forces are not taken into account.

The absorption spectrum of the graphene/Bi_2WO_6 (010) nanocomposite was also calculated, which are determined by the frequency dependent dielectric function

$$\varepsilon(\omega)=\varepsilon_1(\omega)+i\varepsilon_2(\omega) \quad . \tag{1}$$

The imaginary part, $\varepsilon_2(\omega)$, of the dielectric function was calculated from the momentum matrix elements between the occupied and the unoccupied states by the following equation [37]:

$$\varepsilon_2(\omega)=\frac{2e^2\pi}{\Omega\varepsilon_0}\sum_{k,\upsilon,c}\left|\left\langle\psi_k^c\left|\mu r\right|\psi_k^\upsilon\right\rangle\right|^2\delta\left(E_k^c-E_k^\upsilon-E\right) \quad , \tag{2}$$

where Ω, ω, μ, υ, and c are the unit cell volume, photon frequency, and the vectors

defining the polarization of the incident electric field, valence bands, and the conduction bands, respectively. The real part, $\varepsilon_1(\omega)$ is derived from the imaginary part $\varepsilon_2(\omega)$ by means of the Kramers-Kronig transformation, while the absorption coefficient, $I(\omega)$ was derived from $\varepsilon_1(\omega)$ and $\varepsilon_2(\omega)$, as follows[37]:

$$\varepsilon_1(\omega)=1+\frac{2}{\pi}P\int_0^{\infty}\frac{\omega'\varepsilon_2(\omega')}{\omega'^2-\omega_0^2}d\omega' \quad (3)$$

$$I(\omega)=\sqrt{2}\omega\left[\sqrt{\varepsilon_1^2(\omega)+\varepsilon_2^2(\omega)}-\varepsilon_1(\omega)\right]^{\frac{1}{2}} \quad (4)$$

3. Results and discussion

3.1. Surface energies and interface model

To determine the stability of the surface of Bi_2WO_6 (010), we calculated the surface energies of symmetric slab model with a variety of terminals (A, B, C, and D, as shown in Figure 1.) and the different model-thickness. The surface energies E_{sur} can be expressed as:

$$E_{sur}=\left(E_{slab}-\sum_i n_i\mu_i\right)/2S \quad (5)$$

where E_{slab} is the total energy of the slab model, n_i and μ_i(i = Bi, W, O) are the number and chemical potential of Bi, W, and O, respectively, and S (29.68 $Å^2$) is the surface area of the slab model. Under thermal equilibrium growth conditions, the steady production of Bi2WO6 should satisfy the following equation:

$$2\mu_{Bi}+\mu_W+6\mu_O=\mu_{Bi_2WO_6} \quad (6)$$

while thermal equilibrium conditions,

$$\mu_{Bi_2WO_6}=E_{Bi_2WO_6} \quad (7)$$

$$E_{Bi_2WO_6}=2E_{Bi}+E_W+6E_O+\Delta H_f(Bi_2WO_6) \quad (8)$$

where $E_{Bi_2WO_6}$ is the total energy of Bi_2WO_6 for per formula, E_{Bi}, E_W, and E_O are the total energies of per atom for Bi-hexagonal solid, W-cubic solid, and an isolated O_2 molecule, respectively. $\Delta H_f(Bi_2WO_6)$ is the formation enthalpy of per formula of Bi2WO6. Thus, under thermal equilibrium conditions, $\Delta H_f(Bi_2WO_6)$ is expressed as:

$$\Delta H_f(Bi_2WO_6)=2\Delta\mu_{Bi}+\Delta\mu_W+6\Delta\mu_O \quad (9)$$

here, $\Delta\mu_O=\mu_O-E_O$, which is similar for Bi and W. To avoid the precipitation of source elements, μ_i (i = *Bi, W, O*) must satisfy,

$$\Delta\mu_{Bi}<0\ ,\ \Delta\mu_W<0,\ \Delta\mu_O<0 \quad (10)$$

which is smaller than the bulk Bi, V, and O_2 gas, respectively. To avoid the formation

of secondary phases (such as Bi_2O_3, WO_2, and WO_3), $\Delta\mu_i$ (i = Bi, W, O) must further constraints:

$$2\Delta\mu_{Bi}+3\Delta\mu_O<\Delta H_f(Bi_2O_3) \quad (11)$$

$$\Delta\mu_W+2\Delta\mu_O<\Delta H_f(WO_2) \quad (12)$$

$$\Delta\mu_W+3\Delta\mu_O<\Delta H_f(WO_3) \ . \quad (13)$$

Here, the calculated formation enthalpy for Bi_2WO_6 per formula is -15.50 eV. Considering Eqs. (6)-(13), the accessible range for $\Delta\mu_{Bi}$, $\Delta\mu_W$, and $\Delta\mu_O$ is limited and is illustrated as red shades area in Figure 2. In other words, these chemical potentials in the red shades regions are representative of the chemical environment in which Bi_2WO_6 is grown and characterized. In principle, it is allowed for the chemical potentials corresponding to any point at this region. For convenience, we select one representative point labeled as b (O rich) in Figure 2. The calculated values of chemical potentials at point b are -6.09 eV, -24.05 eV, and -4.93 eV for Bi, W, and O, respectively. According to Eq. 2, the calculated surface energies of a variety of slab models for Bi_2WO_6 (010) are listed in Table I. From this table, it can be seen that the surface model C has the lowest energy. Additionally, in order to determine whether the model C surface with 11 atom-layers is stable, the surface energy of the model C surface with 17 and 23 atom-layers are also calculated. We found that a difference of less than 0.00124 $eV\AA^{-2}$ in the model C surface with different layers. This indicates that the C surface model, including at least four relaxed atomic layers, can represent the Bi_2WO_6 (010) surface. Thus, the model C of the Bi_2WO_6 (010) surface is selected to construct the interface model.

To obtain the most stable interface configuration, we optimized various interface models (as Figure 3 (a)) with different initial C-O distances (from 1.0 ~ 4.0 Å) between graphene and Bi_2WO_6 (010) surface. Figure 3(b) shows the optimized geometry structures of the graphene/Bi_2WO_6 (010) nanocomposite with the lowest energy. As seen in this figure, the graphene displays a chiffon-like wavy shape after geometric optimization, which is consistent with experiments observation [19]. This may result from the deformation and distortion during the mixing graphene with Bi_2WO_6 by the strong covalent interaction and chemisorption. This case is different from other graphene-based semiconductor composites (for example, C_3N_4/graphene [38], TiO_2/graphene [39], ZnO_2/graphene [40], Ag_3PO_4/graphene [41], CeO_2/graphene [42], $SrTiO_3$/graphene [43]) where graphene maintains an almost flat C atom layer. Here the

average distance between the C and O atoms is about 1.476 Å, which is consistent to the C-O bond distance (usually 1.42~1.46 Å) of the C-O groups and agrees well with the experimental finding (the ca. 285.8 eV peaks corresponding to C-O bond in the experimental XPS spectra [19-21]). Traditional DFT model for studying chemisorption interfaces has more practical relevance to experimental studies than vdW DFT [38, 44-46]. Thus, we did not consider a traditional vdW interaction forces in this work. The interface adhesion energy was used to judge the adsorption stability of graphene on Bi2WO6 (010) surfaces and was defined as:

$$E_{ad}=(E_{interface}-E_{graphene}-E_{Bi_2WO_6})/S \quad (14)$$

where E_{ad} is the adsorption energy per unit area; $E_{interface}$, $E_{graphene}$, and $E_{Bi_2WO_6}$ are the total energies of the interface, graphene, and Bi_2WO_6 surface, respectively; S (86.53 $Å^2$) is the slab surface area of the interface. The adhesion energy of the graphene/Bi_2WO_6 (010) nanocomposite was calculated to be -0.138 $eVÅ^{-2}$, which indicates that this interface was stable.

3.2. Interface charge transfer.

The calculated Fermi energies of graphene, Bi_2WO_6 (010), and graphene/Bi_2WO_6 (010) nanocomposite are -2.22 eV, -1.15 eV, and -0.33 eV, respectively. The shift of the Fermi energy implies a redistribution of charges after a graphene monolayer is coupled to the Bi_2WO_6 (010) surface. To further understand charge transfer and bonding type, the three-dimensional-charge density-difference with an isosurface value of 0.01 $e/Å^3$ was calculated and is plotted in Figure 4. The cyan and yellow regions represent charge depletion and accumulation in the space, respectively. It can be clearly seen that the charge redistribution fluctuates according to the wave of graphene sheet in the graphene/Bi_2WO_6 (010) composite and mainly occurs at the interface region of the graphene/Bi_2WO_6 (010), whereas there is almost no charge transfer on other layers of Bi_2WO_6 (010) model. This result is slightly different from the case of other graphene/semiconductor composites where the charge merely transfers from one constituent to another or charge redistribution takes place in whole graphene and within several atomic layers of semiconductor [42, 47]. No obvious charge transfer occurred in the second bilayer of the Bi_2WO_6 (010) surface, implying a strong screening of Bi_2WO_6 (010) to adsorbates. A strong charge accumulation is found just above the O atoms in the top layer, whereas the regions of charge depletion appear on the bottom side of the graphene (facing the surface). This indicates that

there is a strong covalent bonding between graphene and Bi_2WO_6 (010) surface, which is in good agreement with the experimental observations [12, 19, 20, 48]. A further Bader charge analysis [49] showed that the total charge transferring from graphene to the top Bi_2WO_6 (010) layer is 2.338 |e|. In the C-O bond of the graphene/Bi_2WO_6 (010) composite, each C atom averagely loses 0.47 |e| and each O atom averagely obtains 0.47 |e|.

The analysis of the work function (WF) for graphene and Bi_2WO_6 (010) surface can help us to understand the origin of the charge transfer in the interface. Our calculated work function of graphene is 4.46 eV vs. vacuum as shown in Figure 5a, which is excellent agreement with previous theoretical calculations (4.42 eV) [50] and experimental value (4.6 eV) [51]. As shown in Figure 5b, the WF of Bi_2WO_6 (010) surface is 7.1 eV, larger than that of graphene. Thus, the spontaneous interfacial charge transfer can be rationalized by the higher work function of the Bi_2WO_6 (010) surface and the electrons will flow from graphene to Bi_2WO_6 (010) after graphene is coupled with Bi_2WO_6 (010) surface. As a consequence, the two phases acquire an equalized E_F. A built-in electric field directed from graphene to the Bi_2WO_6 (010) will be established, which can stop the charge continue to diffusion between graphene and Bi_2WO_6 (010). The E_F of graphene shifts downward by 1.02 eV, while the E_F of Bi_2WO_6 (010) shifts upward by 1.62 eV. Therefore, Bi_2WO_6 (010) is negatively charged and graphene is positively charged near the interface due to electrostatic induction, resulting in a net efficient electrons depletion at the graphene, as shown in the result of charge-density-difference (Figure 4).

3.3. Electronic structures.

To understand the microscopic mechanism of enhanced photocatalytic efficiency，the layer-resolved density of states (DOS) for the Bi_2WO_6 (010) surface are depicted in Figure 6a. It is found that the Fermi level is pinned inside some valence states, indicating p-type feature and upward band-bending. It is noted that these states are not strictly confined to the first layer of surface and spreads out into several top and bottom layers of the Bi_2WO_6 (010) slab. Furthermore, the disproportional electronic states near the Fermi level is triggered. This can be attributed to, at the top and bottom surface, the surface states caused by the different atomic or electronic surface reconstruction of the off-stoichiometric Bi_2WO_6 (010) slab model. Thus, partially

filled bands appear in pure Bi_2WO_6 (010) surface, which will lead to recombination centers and thus is unfavorable for photocatlysis.

To explore the effect of graphene coupling to Bi_2WO_6 (010) on photocatalytic efficiency, we also calculated the layer-resolved DOS of the graphene/Bi_2WO_6 (010) and plotted them in Figure 6b. As seen in this figure, once graphene is introduced to Bi_2WO_6 (010) surface, the C orbitals strongly hybrid with the orbitals of outmost-layer O atoms of Bi_2WO_6 (010). It indicates the presence of strong interfacial interactions between graphene and Bi_2WO_6 (010) surface, consisting with the result of charge-density-difference mentioned above in Section 3.2. On the other hand, the valence bands of the first layer in Bi_2WO_6 (010) shift to higher energy, while the surface states of the second and third layers have vanished. Moreover, the electronic orbital of W atom at conduction band of graphene/Bi_2WO_6 (010) shift to lower energy by about 0.5 and 0.75 eV compared with Bi_2WO_6 (010) surface and bulk Bi_2WO_6 [6], respectively. Simultaneously, some mixing states between C and O appear at the bottom of conduction band of Bi_2WO_6 (010). These changes can be ascribed to C-O covalent bonds and surface reconstruction induced by the introducing of graphene. At the interface of graphene/Bi_2WO_6 (010), the bands of Bi_2WO_6 (010) bend upward to graphene and a build-in electric field directed from graphene to Bi_2WO_6 (010) is established, and thus the photogenerated electrons produced by Bi_2WO_6 (010) surface was promoted to move to graphene. At the same time, the photogenerated electrons produced by inside Bi_2WO_6 (010) will diffuse to the surface. Therefore, the photogenerated electron-hole pairs can be separated efficiently, which will improve photocatalytic activity after graphene was introduced into Bi_2WO_6 (010).

3.4. Optical properties

In general, the optical absorption properties of semiconductor photocatalysts are closely related to their electronic structures and are of great importance to its photocatalytic activity. To examine the effect on the photocatalytic efficiency of the Bi_2WO_6 (010) coupled with graphene, the calculated UV-vis absorption spectra of pure Bi_2WO_6 and the graphene/Bi_2WO_6 (010) heterojunction are plotted in Figure 7. Compared to pure Bi_2WO_6, the optical absorption edge clearly red-shifted to a longer wavelength region and a slightly higher absorption intensity has been observed in the visible-light region for the whole graphene/Bi_2WO_6 (010) heterojunction. Combining with the calculated layer-resolved DOS for graphene/Bi_2WO_6 (010), the relevant absorption of Bi_2WO_6 (010) top surface only play an additional role, while the

majority of light adsorption still happens inside the slab. Simultaneously, due to the presence of strong interfacial interactions between graphene and Bi_2WO_6 (010) surface, linear band structure of the pristine graphene is disrupted and small energy-gaps appear. Thus, these absorptions corresponding to the interband transition of graphene would cause the absorption spectrum of the graphene/Bi_2WO_6 (010) covering the entire visible-light region and even infrared-light region. Therefore, the red-shift of absorption edge and a slightly higher absorption intensities in the visible-light region could be ascribed to the light adsorption of Bi_2WO_6 (010) bottom surface and graphene.

3.5. photocatalytic mechanism.

The CB and VB edge positions of a semiconductor at the point of zero charge (E^0_{CB}, E^0_{VB}) can be expressed [52]

$$E^0_{CB}=\chi(S)-E^0-\frac{1}{2}E_g \quad (15)$$

$$E^0_{VB}=E^0_{CB}+E_g \quad (16)$$

where the $\chi(S)$ is the absolute electronegativity of the semiconductor (i.e., the geometric mean of the constituent atoms) [53], E_g is the band gap, and E^0 is the scale factor relating the reference electrode redox level to the absolute vacuum scale (AVS) (E^0 ~ 4.5 eV for a normal hydrogen electrode (NHE)). The calculated E^0_{CB} and E^0_{VB} of Bi_2WO_6 (010) are 2.49 eV and -0.31 eV [6], respectively. According to relation between E_{NHE} and E_{AVS} ($E_{AVS}=-E_{NHE}-E^0$), the E_{AVS} of the CB and VB edges of Bi_2WO_6 are estimated to be -4.19 and -6.99 eV, respectively. Because of the strong chemical interaction between graphene and Bi_2WO_6 (010), the band edge positions of the graphene/Bi_2WO_6 (010) will change. The calculated E_{AVS} of the CB and VB edges of the graphene/Bi_2WO_6 (010) are -3.81 and -6.01 eV, respectively. Thus, the conduction band potential of graphene/Bi_2WO_6 (010) are upward (more negative) by 0.38 V compared with pure Bi_2WO_6, which is in agreement with experimental Mott-Schottky measurements [19, 21], explaining why the graphene/Bi_2WO_6 shows good activity in H_2 production and a stronger reductive power.

On the basis of above results, the change in E_F and the charge transfer at the interface under light irradiation for the graphene/Bi_2WO_6 (010) nanocomposite are plotted in Figure 8. As shown in Figure 8 (left), because the E_F of graphene is higher than that of Bi_2WO_6 (010), the electron will transfer from graphene to Bi_2WO_6 (010) when they are coupled. The transfer will stop and the charge equilibration will reach

when the position of E_F of graphene become same to that of Bi_2WO_6 (010). While the CB bottom position of Bi_2WO_6 (010) is still higher than the E_F of graphene. A built-in electric field directed from graphene to Bi_2WO_6 (010) will established simultaneously. Under visible-light irradiation, Bi_2WO_6 (010) absorb photons with greater energy than the corresponding band gap energy, and then electrons in the VB will be excited to the CB leaving holes in the VB. The photogenerated electrons produced by Bi_2WO_6 (010) will be injected into the graphene due to the higher CB bottom position of Bi_2WO_6 (010) and the built-in electric field between graphene and Bi_2WO_6 (010), leaving holes on the VB of Bi_2WO_6 (010), as shown in Figure 8 (right). Owing to the two-dimensional conjugated π structure and superior electrical conductivity of graphene, the photogenerated electrons could quickly transfer to the surface of graphene and participate in the reduction reaction. It illustrates that graphene could serve as electron captors and transporters, effectively enhancing charge separating and suppressing charge recombination. An effective separation of photogenerated electron-hole pairs and fast interfacial charge transfer have been confirmed by the experimental electrochemical impedance spectroscopies (EIS) and photoluminescence spectra for graphene/Bi_2WO_6 (010) [19-21]. Therefore, the photocatalytic reactions are allowed to take place not only on the surfaces of Bi_2WO_6, but also on graphene with greatly expanded reaction sites.

4. Conclusions

The stability, electronic structure, charge transfer, and optical properties of graphene/Bi_2WO_6 (010) nanocomposite were studied by using the density functional theory. The mechanism of enhanced photocatlytic activity for the graphene/Bi_2WO_6 (010) composite are explored. It is found that graphene can couple with the Bi_2WO_6 (010) surface with strong covalent C-O interaction. In addition, the linear band structure is disrupted and small bandgaps appear for graphene when graphene is combined with Bi_2WO_6 (010). The absorption edge red-shifts to entire visible-light region and even infrared-light region. The photogenerated electrons can be injected into graphene from the conduction band of Bi_2WO_6 (010) surface under the built-in electric field and band edge potential well after graphene is coupled with Bi_2WO_6 (010) surface. Consequently, the photogenerated electrons move to the surface of graphene and the holes leave on the surface of Bi_2WO_6 (010), which significantly reduces the probability of electron-hole recombination and increases catalytic reaction sites. Our results reveal the interface effect on photogenerated electron-holes

separation and charge transfer in graphene/Bi_2WO_6 (010). It shows a possibility for the utilization of low-cost graphene as a substitute for noble metals deposited on photocatalyst to develop high-performance photcatalyst.

Acknowledgments

This research is sponsored by the National Natural Science Foundation of China (nos. 11547011, 51571083, 51371076, and 21303027), Excellent Doctoral Dissertation breeding program of Henan University (no.Y1317011), the Program for Innovative Research Team in the University of Henan Province (no. 13IRTSTHN017), the Henan International Science and Technology Cooperation Project (no.144300510077 and 162102410013), the NSF from department of education of Guizhou province (no. QJHKY[2014]306, QJTD[2013]16), and the Program for Innovative Research Team of Guizhou Province (No. QKTD[2014]4021).

Reference

1. X. Chen and S. S. Mao, *Chem. Rev.*, 2007, **107**, 2891-2959.
2. A. Kudo and Y. Miseki, *Chem. Soc. Rev.*, 2009, **38**, 253-278.
3. J. Liu, H. Wang, S. Wang and H. Yan, *Mater. Sci. Eng., B*, 2003, **104**, 36-39.
4. T. Saison, N. Chemin, C. Chanéac, O. Durupthy, V. r. Ruaux, L. Mariey, F. o. Maugé, P. Beaunier and J.-P. Jolivet, *J. Phys. Chem. C*, 2011, **115**, 5657-5666.
5. C.-M. Liu, J.-W. Liu, G.-Y. Zhang, J.-B. Zhang, Q.-S. Wu, Y.-Y. Xu and Y.-Q. Sun, *RSC Adv.*, 2015, **5**, 32333-32342.
6. F. Ren, J. Zhang and Y. Wang, *RSC Adv.*, 2015, **5**, 29058-29065.
7. T. Saison, P. Gras, N. Chemin, C. Chaneac, O. Durupthy, V. Brezova, C. Colbeau-Justin and J. P. Jolivet, *J. Phys. Chem. C*, 2013, **117**, 22656-22666.
8. S. Z. Wei, S. Liu, L. Michelle, S. Y. Zhang, Z. Liu, M. Adnen and M. Y. Han, *Adv. Mater.*, 2012, **24**, 2310-2314.
9. R. Jia, W. Wang, S. Sun, Z. Ling and C. Jiang, *Appl. Catal. B*, 2009, **90**, 50-55.
10. M. Qamar, R. B. Elsayed, K. R. Alhooshani, M. I. Ahmed and D. W. Bahnemann, *ACS Appl. Mater. Interfaces*, 2015, **7**, 1257-1269.
11. Q. Xiang, J. Yu and M. Jaroniec, *Chem. Soc. Rev.*, 2012, **41**, 782-796.
12. J. J. Ding, W. H. Yan, W. Xie, S. Sun, J. Bao and C. Gao, *Nanoscale*, 2014, **6**, 2299-2306.
13. S.-P. Hu, C.-Y. Xu and L. Zhen, *Mater. Lett.*, 2013, **95**, 117-120.
14. S. Obregón and G. Colón, *Appl. Catal. B*, 2013, **140-141**, 299-305.
15. T. H. Ji, M. Sun and P. Han, *New Carbon Mater.*, 2013, **28**, 401-407.
16. N. Zhang, Y. Zhang and Y. J. Xu, *Nanoscale*, 2012, **4**, 5792-5813.
17. Y. L. Min, K. Zhang, Y. C. Chen and Y. G. Zhang, *Sep. Purif. Technol.*, 2012, **86**, 98-105.
18. H. W. Ma, J. F. Shen, M. Shi, X. Lu, Z. Q. Li, Y. Long, N. Li and M. X. Ye, *Appl. Catal. B*, 2012, **121**, 198-205.

19. Z. Sun, J. Guo, S. Zhu, L. Mao, J. Ma and D. Zhang, *Nanoscale*, 2014, **6**, 2186-2193.
20. Y. Zhou, X. J. Zhang, Q. Zhang, F. Dong, F. Wang and Z. Xiong, *J. Mater. Chem. A*, 2014, **2**, 16623-16631.
21. E. P. Gao, W. Z. Wang, M. Shang and J. H. Xu, *Phys. Chem. Chem. Phys.*, 2011, **13**, 2887-2893.
22. J. J. Xu, Y. H. Ao and M. D. Chen, *Mater. Lett.*, 2013, **92**, 126-128.
23. P. E. Blöchl, *Phys. Rev. B*, 1994, **50**, 17953-17979.
24. G. Kresse and J. Hafner, *Phys. Rev. B*, 1993, **47**, 558-561.
25. G. Kresse and J. Furthmüller, *Phys. Rev. B*, 1996, **54**, 11169-11186.
26. J. P. Perdew and Y. Wang, *Phys. Rev. B*, 1992, **45**, 13244-13249.
27. J. P. Perdew, K. Burke and M. Ernzerhof, *Phys. Rev. Lett.*, 1996, **77**, 3865-3868.
28. N. I. Medvedeva, V. P. Zhukov, V. A. Gubanov, D. L. Novikov and B. M. Klein, *J. Phys. Chem. Solids*, 1996, **57**, 1243-1250.
29. A. Walsh, G. W. Watson, D. J. Payne, R. G. Edgell, J. Guo, P.-A. Glans, T. Learmonth and K. E. Smith, *Phys. Rev. B*, 2006, **73**.
30. K. S. Knight, *Mineral. Mag.*, 1992, **56**, 399-409.
31. H. J. Monkhorst and J. D. Pack, *Phys. Rev. B*, 1976, **13**, 5188-5192.
32. J. Neugebauer and M. Scheffler, *Phys. Rev. B*, 1992, **46**, 16067-16080.
33. G. Makov and M. C. Payne, *Phys. Rev. B*, 1995, **51**, 4014-4022.
34. S. L. Dudarev, G. A. Botton, S. Y. Savrasov, C. J. Humphreys and A. P. Sutton, *Phys. Rev. B*, 1998, **57**, 1505-1509.
35. H. Kamisaka, T. Suenaga, H. Nakamura and K. Yamashita, *J. Phys. Chem. C*, 2010, **114**, 12777-12783.
36. J. Heyd, G. E. Scuseria and M. Ernzerhof, *J. Chem. Phys.*, 2006, **124**, 219906.
37. A. J. Read and R. J. Needs, *Phys. Rev. B*, 1991, **44**, 13071-13073.
38. X. Li, Y. Dai, Y. Ma, S. Han and B. Huang, *Phys. Chem. Chem. Phys.*, 2014, **16**, 4230-4235.
39. H. T. Gao, X. H. Li, J. Lv and G. J. Liu, *J. Phys. Chem. C*, 2013, **117**, 16022-16027.
40. P. Xu, Q. Tang and Z. Zhou, *Nanotechnology*, 2013, **24**, 305401.
41. L. Xu, W. Q. Huang, L. L. Wang, G. F. Huang and P. Peng, *J. Phys. Chem. C*, 2014, **118**, 12972-12979.
42. L. Xu, W. Q. Huang, L. L. Wang and G. F. Huang, *ACS Appl. Mater. Interfaces*, 2014, **6**, 20350-20357.
43. Y. C. Yang, L. Xu, W. Q. Huang, C. Y. Luo, G. F. Huang and P. Peng, *J. Phys. Chem. C*, 2015, **119**, 19095-19104.
44. J. E. Padilha, A. Fazzio and A. J. da Silva, *Phys. Rev. Lett.*, 2015, **114**, 066803.
45. C. Gong, G. Lee, B. Shan, E. M. Vogel, R. M. Wallace and K. Cho, *J. Appl. Phys.*, 2010, **108**, 123711.
46. X. Zhang, W. Mi, X. Wang, Y. Cheng and U. Schwingenschlogl, *Sci. Rep.*, 2014, **4**, 7368.
47. A. Du, Y. H. Ng, N. J. Bell, Z. Zhu, R. Amal and S. C. Smith, *J. Phys. Chem. Lett.*, 2011, **2**, 894-899.
48. E. Gao, W. Wang, M. Shang and J. Xu, *Phys. Chem. Chem. Phys.*, 2011, **13**, 2887-2893.

49. W. Tang, E. Sanville and G. Henkelman, *J. Phys.: Condens. Matter*, 2009, **21**, 084204.
50. R. Czerw, B. Foley, D. Tekleab, A. Rubio, P. M. Ajayan and D. L. Carroll, *Phys. Rev. B*, 2002, **66**.
51. S. Suzuki, C. Bower, Y. Watanabe and O. Zhou, *Appl. Phys. Lett.*, 2000, **76**, 4007.
52. S. R. Morrison, *Electrochemistry at Semiconductor and Oxidized Metal Electrodes*, Plenum Press, New York, NY, USA, 1980.
53. R. T. Sanderson, *Chemical Periodicity*, Reinhold, New York, NY, USA, 1960.

Table 1. Calculated surface energies (eV/Å^{-2}) for Bi_2WO_6 (010) termination (A, B, C, D) slab as a function of slab thickness (7, 9, 11, 13, 14, 15, 17, and 23 atom layers).

Terminate / Atom layers	A	B	C	D
7	0.113615494			0.248975749
9		0.100084711		
11			0.013304695	
13				0.2465356
14	0.11198159			
15		0.095438504		
17			0.013937482	
23			0.015184526	

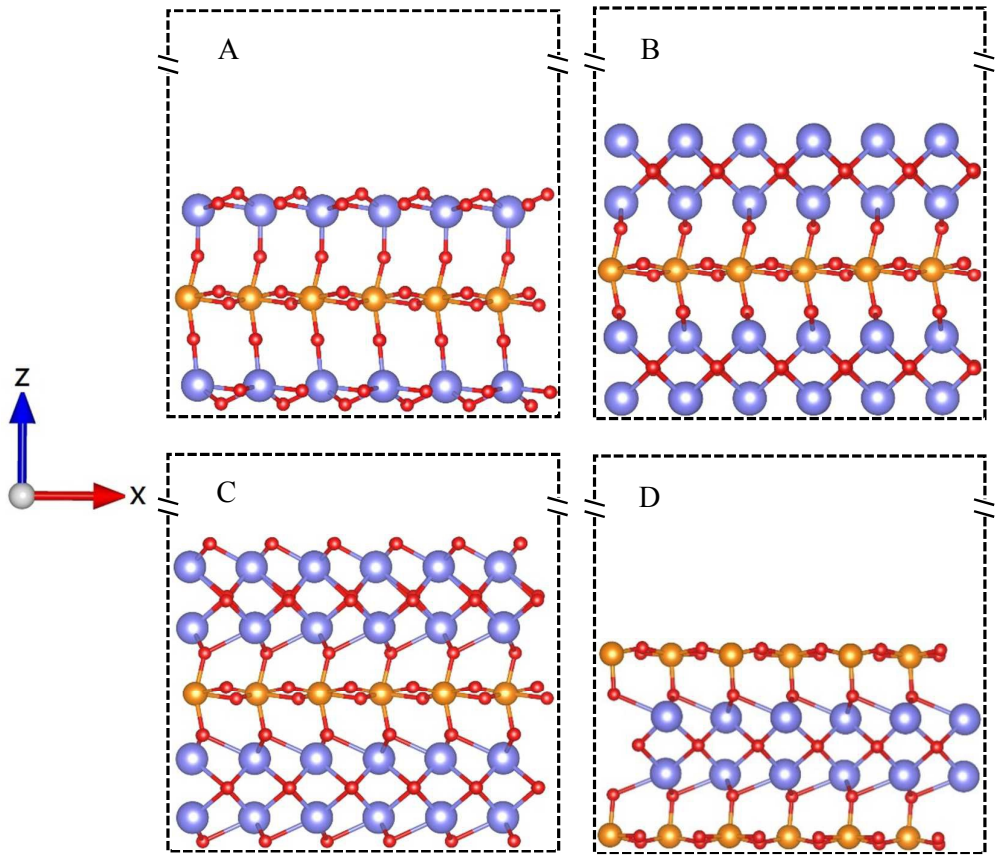

Figure 1. (Color online) Frontal view of optimized four different symmetric terminals of 3×1 Bi_2WO_6 (010) slab. The red, orange, and light blue spheres represent O, W, and Bi atoms, respectively.

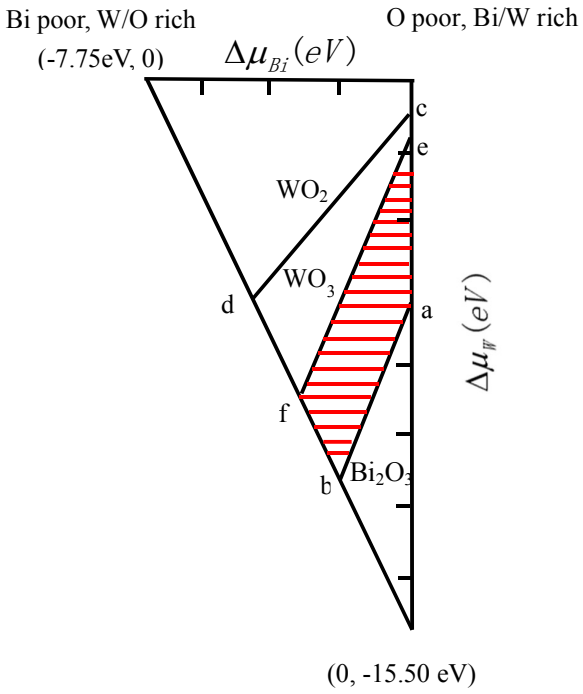

Figure 2. (Color online) Accessible range of chemical potentials (red shades region) for equilibrium growth conditions of Bi_2WO_6. Specific point b is chosen as the representative chemical potential for the following surface energy calculation, in which the b condition is O rich.

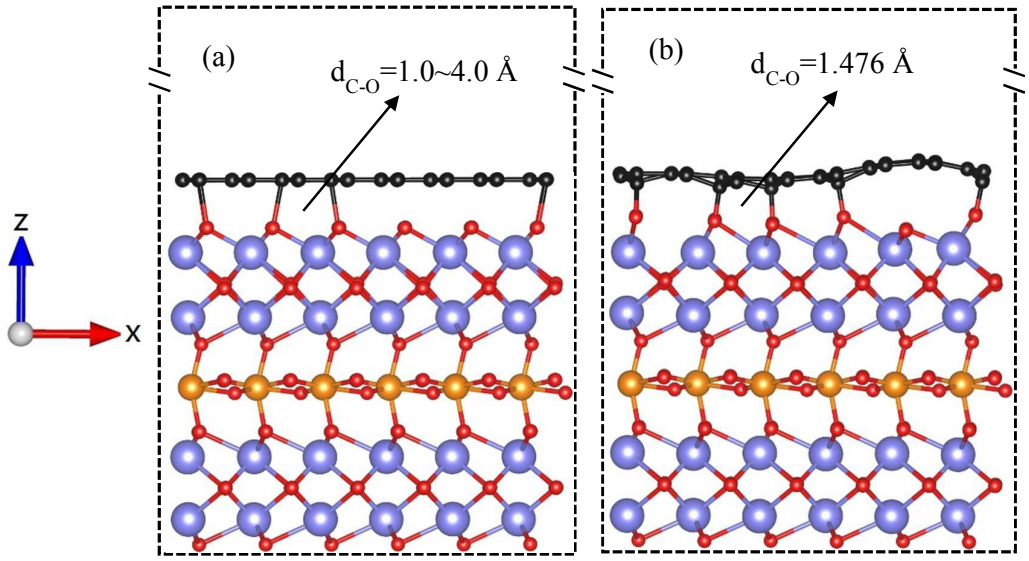

Figure 3. (Color online) Models simulating the graphene/Bi_2WO_6 (010) nanocomposite before geometric optimization (a) and after geometric optimization (b). The red, orange, purple, and black spheres represent O, W, Bi, and C atoms, respectively.

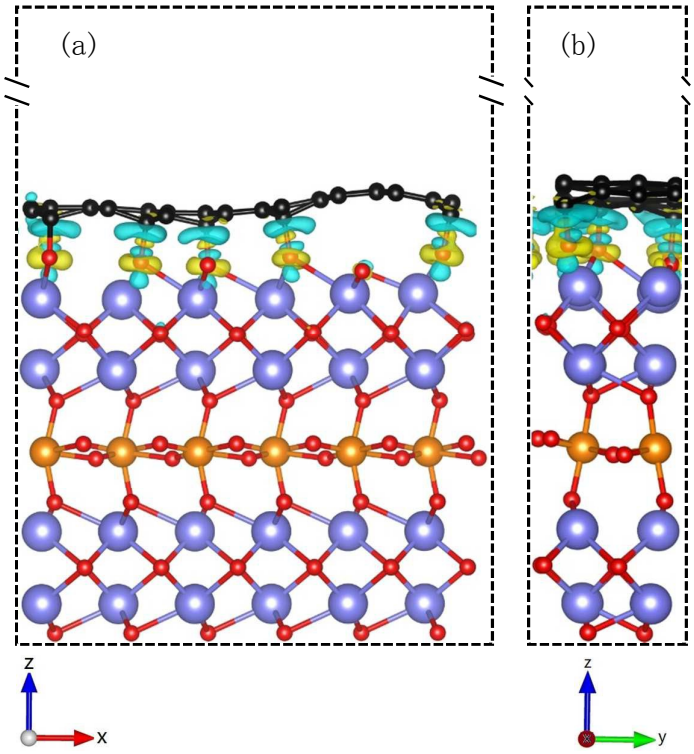

Figure 4. (Color online) The different three-dimensional charge densities for the graphene/Bi_2WO_6 (010) nanocomposite with an isovalue of 0.01 eÅ^{-3} (from the frontal view (a) and the lateral view (b)). The cyan and yellow regions represent the charge depletion and accumulation in the space, respectively. The labeling of the atoms is the same as in Figure 3.

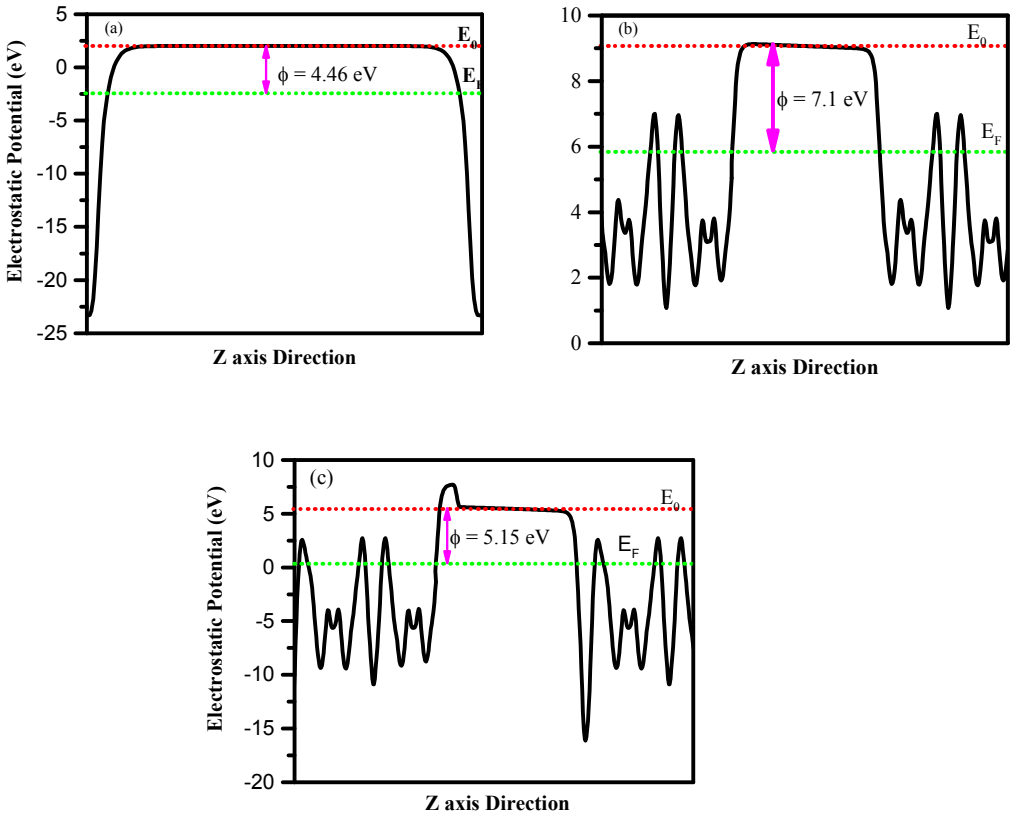

Figure 5. (Color online) The electrostatic potentials for (a) the graphene, (b) Bi_2WO_6 (010) surface, and (c) graphene/Bi_2WO_6 (010) nanocomposite. The red and green dashed lines represent the vacuum level (E_o) and the Fermi level (E_F), respectively. The ø is the work function.

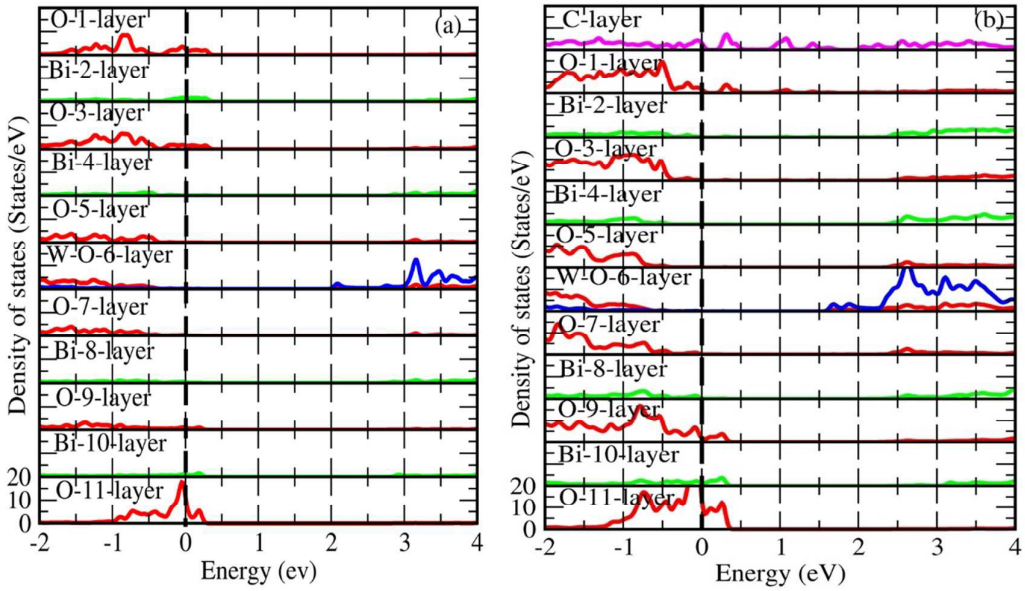

Figure 6. (Color online) Calculated layer-resolved density of states (DOS) for (a) Bi_2WO_6 (010) surface and (b) graphene/Bi_2WO_6 (010) nanocomposite. The red, green, magenta, and bule lines represent the DOS of O, Bi, and W, respectively. The zero of the energy is set at E_F.

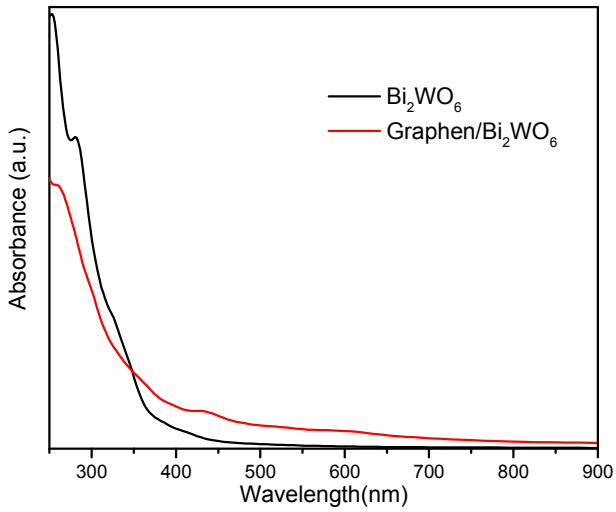

Figure 7. (Color online) Calculated optical absorption spectras of Bi_2WO_6 and Graphene/Bi_2WO_6 (010) nanocomposite as a function of wavelength.

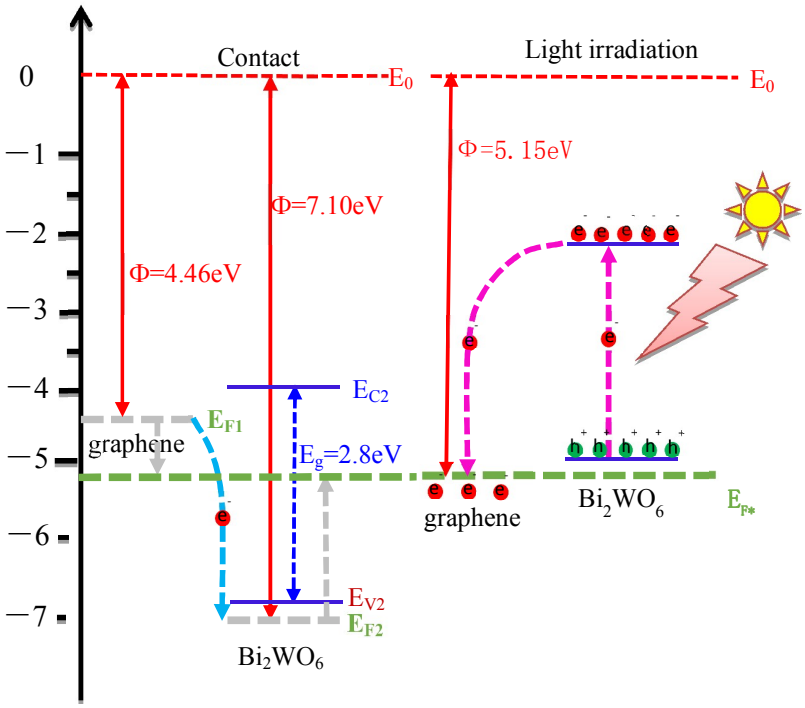

Figure 8. (Color online) A schematic diagram of the Fermi level change and the charge transfer at the interface under light irradiation for the graphene/Bi_2WO_6 (010) nanocomposite; ø is the work function, E_C is the bottom of the conduction band, E_V is the top of the valence band, E_g is the band gap, and E_{F1}, E_{F2}, and E_{F*} are the Fermi levels of graphene, Bi_2WO_6, and graphene/Bi_2WO_6 (010) nanocomposite, respectively.